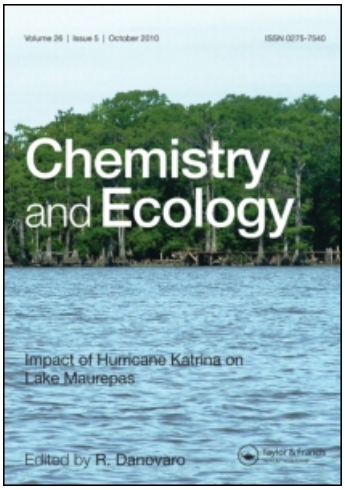

Chemistry and Ecology
Publication details, including instructions for authors and subscription information:
http://www.informaworld.com/smpp/title~content=t713455114

Submarine diagenetic products on the sediment-starved Gorgona slope, Tuscan Archipelago (Tyrrhenian Sea)

Alessandro Remia[a]; Paolo Montagna[b]; Marco Taviani[a]
[a] ISMAR—Marine Geology Division, CNR, Bologna, Italy [b] Department of Mineralogy and Petrology, University of Padua, Padua, Italy

To cite this Article Remia, Alessandro , Montagna, Paolo and Taviani, Marco(2004) 'Submarine diagenetic products on the sediment-starved Gorgona slope, Tuscan Archipelago (Tyrrhenian Sea)', Chemistry and Ecology, 20: 3, 131 — 153
To link to this Article: DOI: 10.1080/02757540310001642823
URL: http://dx.doi.org/10.1080/02757540310001642823

Chemistry and Ecology
June 2004, Vol. 20 (Supplement 1), pp. S131–S153

Taylor & Francis
Taylor & Francis Group

SUBMARINE DIAGENETIC PRODUCTS ON THE SEDIMENT-STARVED GORGONA SLOPE, TUSCAN ARCHIPELAGO (TYRRHENIAN SEA)

ALESSANDRO REMIA[a,*], PAOLO MONTAGNA[b] and MARCO TAVIANI[a]

[a]*ISMAR—Marine Geology Division, CNR, via Gobetti 101, I-40129 Bologna, Italy;*
[b]*Department of Mineralogy and Petrology, University of Padua, Corso Garibaldi 37, I-35137 Padua, Italy*

Various types of submarine diagenetic products occur at bathyal depths (>300 m) along the Gorgona slope, eastern Tyrrhenian Sea. Bottom sampling during cruise LM-99 of the R/V *Urania* recovered pristine to diagenetic altered shells (including *steinkern*) and phosphatized/carbonate hardgrounds. Chemical maps (Al, Ca, Si, S, Fe, P) are provided to characterize these diagenetic products. A peculiar category of *steinkern* (black molds) of benthic invertebrate calcareous shells is the result of pervasive substitution by phosphomicrite and glaucony. Chemical precipitation and mineral replacement at the expense of pelagic sediment and skeletal carbonates took place under prolonged conditions of exposure at the seawater–sediment interface.

Keywords: Submarine diagenesis; Deep sea; Tyrrhenian Sea; Hardgrounds; Skeletal carbonates; Chemical maps

1 INTRODUCTION

Sediment-starved deep-sea environments of semi-enclosed and marginal basins are notable sites of peculiar submarine diagenetic processes, often promoting the partial or complete dissolution of existing carbonates as well as the formation of carbonate and phosphatic hardgrounds through inorganic- and/or biological-mediated processes (*e.g.* Milliman and Müller; 1973; Rezak, 1974; Milliman, 1974, 1977; Baturin, 1981; Bernoulli and McKenzie, 1981; Groupe Escarmed, 1983; Von Rad and Rösch, 1984; Allouc, 1986, 1990; Brachert and Dullo, 1990, 1991; Wilber and Neumann, 1993; Hofmann *et al.*, 1998; Taviani, 1998).

The complex submarine topography of the Tyrrhenian Sea, punctuated by seamounts, offshore banks and steep canyons, includes a number of situations conducive to the formation of chemical sediments and diagenetic products (*e.g.* Selli, 1970; Shonting and Bartolini, 1971; Allouc, 1990; Brachert and Dullo, 1990).

Cruise LM-99 aboard the R/V *Urania* in the Eastern Tyrrhenian Sea was designed to study deep-sea biogenic carbonate deposits, including aphotic coral banks (Remia and Taviani, 2003). Considerable attention was devoted to surveying the Gorgona slope, forming the eastern shoulder of a NNW–SSE depression about 25 nautical miles in length, the maximum

* Corresponding author.

ISSN 0275-7540 print; ISSN 1029-0370 online
DOI: 10.1080/02757540310001642823

depth of which slightly exceeds 600 m (Fig. 1). Dredge and gravity core samples from the eastern part of the Gorgona slope provided various examples of diagenetic products such as phosphatized and carbonate hardgrounds, as well as body fossils and *steinkern* (molds) of skeletal parts belonging to different marine calcareous invertebrates. In particular, sampling along the slope between 300 and 460 m consistently recovered predominantly muddy sediments entrapping a mixture of lithified slabs and shelly remains (St. LM99-86 and 110). Preservation of such fossil remains varies greatly, including both pristine and diagenetically altered skeletal parts, whose original minerals have been replaced by other mineral phases (molds). The bulk of the catch consisted of skeletal remains attributable to extant taxa probably datable to the last glacial age (Fig. 4), as supported by the occurrence of cold Pleistocene index-fossils (*i.e. Pseudamussium septemradiatum*). These skeletal assemblages appear diverse and dominated by infaunal and semi-infaunal bivalves (*e.g. Astarte sulcata*, *Venus casina*, etc.), gastropods, scaphopods, bryozoans (*e.g. Turbicellepora coronopus*), brachiopods (*e.g. Gryphus vitreus*) and scleractinian corals (*e.g. Caryophyllia smithii*).

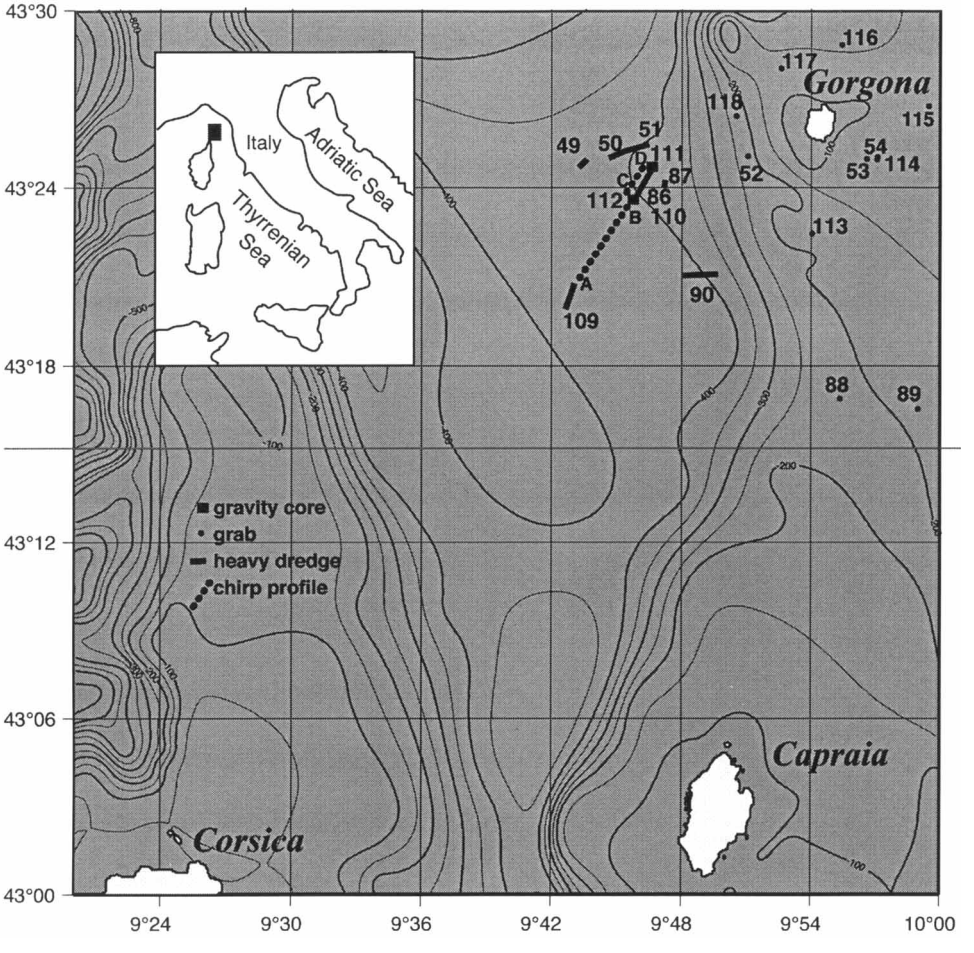

FIGURE 1 Location map of the eastern Tyrrhenian Sea showing cruise LM-99 sample stations and selected chirp-sonar profiles tracks on the Gorgona slope.

Surprisingly, numerous shells of late Miocene age (Messinian) embedded within greenish marls were also recovered mixed together with the Pleistocene lithologies. This Messinian assemblage consists mostly of brackish bivalves of the family Limnocardiidae (*e.g. Limnocardium*), the gastropod *Melanopsis* (Taviani *et al.*, 2002) and ranges from recrystallized molds to chalky shells. In this sector of the Mediterranean basin, brackish pre- and post-evaporitic Messinian deposits crop out in Corsica and Tuscany (*e.g.* Gillet *et al.*, 1977; Magné *et al.*, 1977; Bossio *et al.*, 1978; Benvenuti *et al.*, 1994, 2001; Ghetti *et al.*, 2002) and have been recorded in the Tyrrhenian Sea South of our area (Bacini Sedimentari, 1979; Aleria, 1980). Messinian deposits contribute to make up the sedimentary successions constituting the eastern side of the Gorgona slope, and these strata are at places exposed at the water–sea

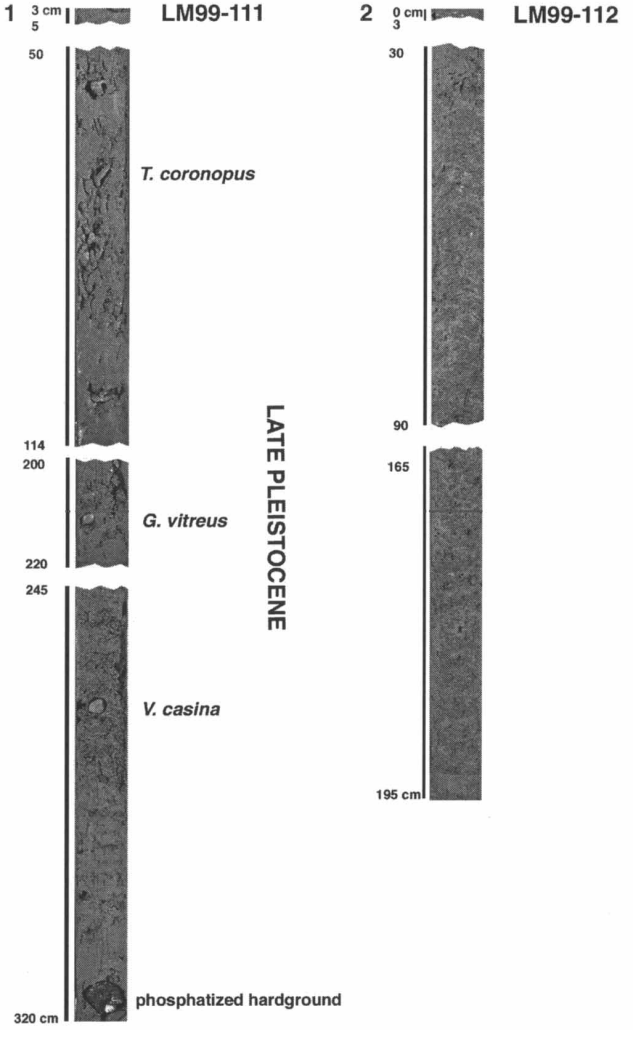

FIGURE 2 LM-99 gravity cores collected on the eastern side of the Gorgona slope along the same profile of dredge St. LM99-110: (1) Core LM99-111 consists of gray sandy muds and mud containing cold Pleistocene (possibly last glacial) macrofossils, including large morphotypes of the bryozoan *Turbicellepora coronopus*; note the presence of a hardground pebble near the core bottom; (2) Core LM99-112 consists of homogenous gray to greenish silty muds.

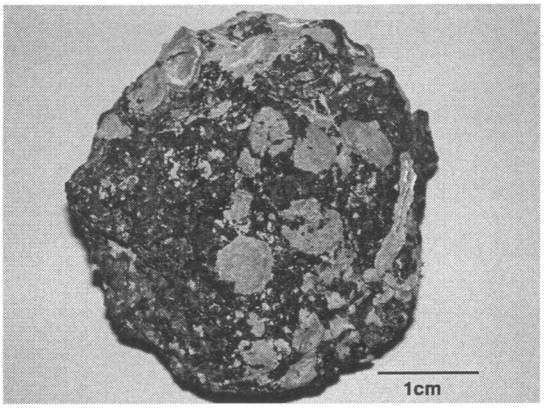

FIGURE 3 Example of hardground slabs recovered at St. LM99-110; most slabs are variously encrusted by calcareous epifauna, typically serpulid polychaetes, and affected by microborers (*Trypanites* ichnofacies).

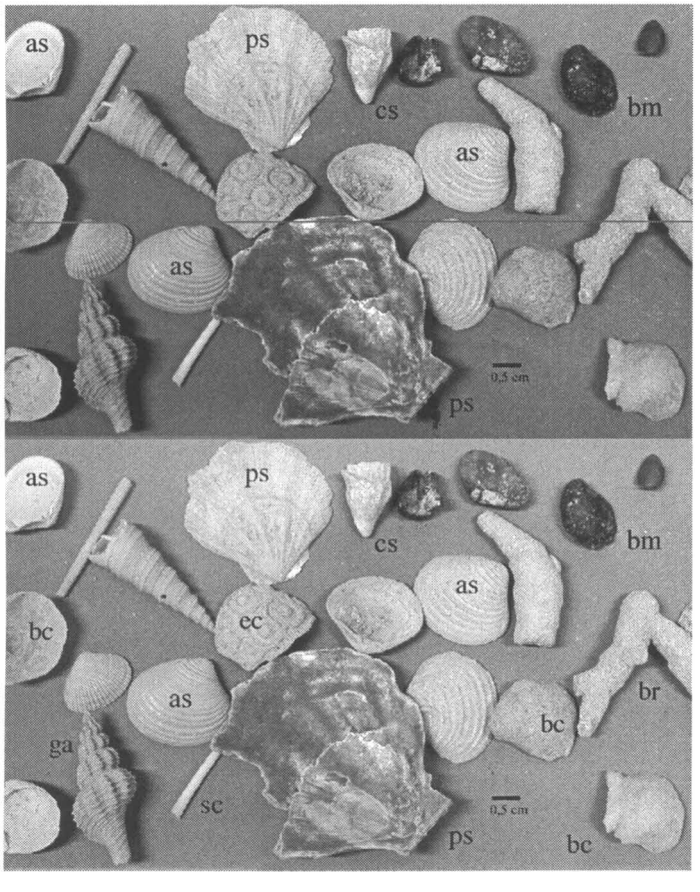

FIGURE 4 Example of a cold-Pleistocene skeletal calcareous assemblage from St. LM99-86 containing bivalves (*e.g. Astarte sulcata* = as, and the cold guest *Pseudamussium septemradiatum* = ps), gastropods = ga, scaphopods = sc, brachiopods = bc, bryozoans (*e.g. Turbicellepora coronopus* = br), scleractinian corals (*Caryophyllia smithii* = cs), echinoids = ec, etc. Preservation state of such material varies greatly ranging from pristine to diagenetically altered and microbored (*Trypanites* facies) *steinkern* (black molds = bm).

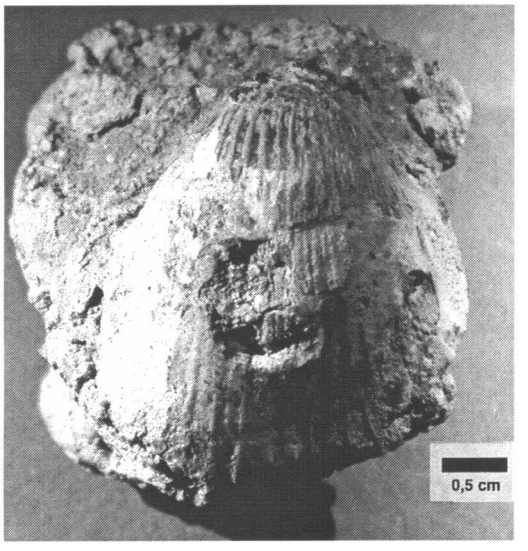

FIGURE 5 Fossiliferous concretion cementing a bivalve shell belonging to upper Miocene (Messinian) assemblages (brackish-water Limnocardiid).

floor interface. However, the slope stratigraphy is primarily represented by muddy deposits of Pleistocene age, as evidenced in gravity cores (St. LM99-111: Fig. 2).

The scope of this article is to report on the most relevant petrographic and chemical aspects of some remarkable examples of submarine diagenetic products within a terrigeneous-sediment starved deep-sea setting, recovered during cruise LM99. Examples of (1) hard-grounds (Fig. 3), (2) well-preserved Pleistocene skeletal parts (Fig. 4), concretions (Fig. 5), and (3) bivalve molds (Fig. 6) have been analyzed to shed light on their mineralogical,

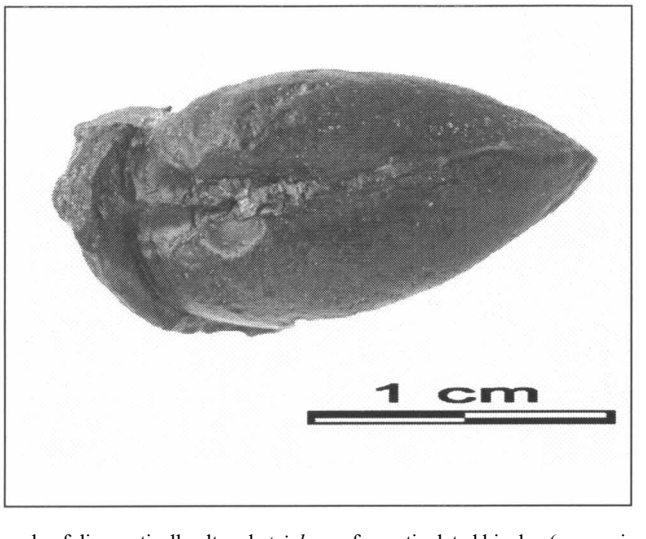

FIGURE 6 An example of diagenetically altered *steinkern* of an articulated bivalve (upper view); the original shell is completely replaced by phosphomicrite and glaucony (black mold).

petrographic and chemical attributes as a contribution to the understanding of chemical sedimentation under prolonged sea-bottom exposure.

2 MATERIAL AND METHODS

The area under study was first imaged through chirp-sonar seismics (Fig. 7) to assist the sampling strategy which, in turn, consisted of 2 gravity cores, 8 heavy dredge and 11 grab samples collected at a depth range of 134–620 m (Tab. I). Sediment sub-samples from stations were washed over a set of standard sieves and the fraction coarser than 2 mm inspected for its content. When present, various types of lithified crusts, slabs, fossiliferous concretions, individual shell remains and molds, were selected for mineralogical, petrographic and chemical investigations in the laboratory.

Hardground fragments and Messinian concretions were sectioned by means of a diamond blade, ground to 30 μm and polished using alumina powder. The same operation was carried out on *Astarte sulcata* (bivalve) shell fragments, *Caryophyllia* (scleractinian coral) and pieces of bivalve molds (*steinkern*) previously impregnated with epoxy resin in order to keep fragile internal microstructures intact.

In addition, fractured sections were gold-coated and investigated using a CamScan MX 2500 scanning electron microscope (SEM) to define the internal microstructures of the bioclasts better.

Qualitative and semi-quantitative mineral analyses were done by X-ray diffraction using a single crystal of silicon as a sample holder (Plate 1). Use of this sample holder improves basic identification of characteristic peaks or reflections of the analyzed minerals from the analytic background. Samples characterized by a minor amount of clay minerals compared to the carbonate fraction were soaked in a hydrochloric acid solution (8%) in order to dissolve the calcium carbonate. Some of them underwent an ethylene glycol solvation for the identification of smectites by the expansion and contraction of the 001 smectite peak. Fine

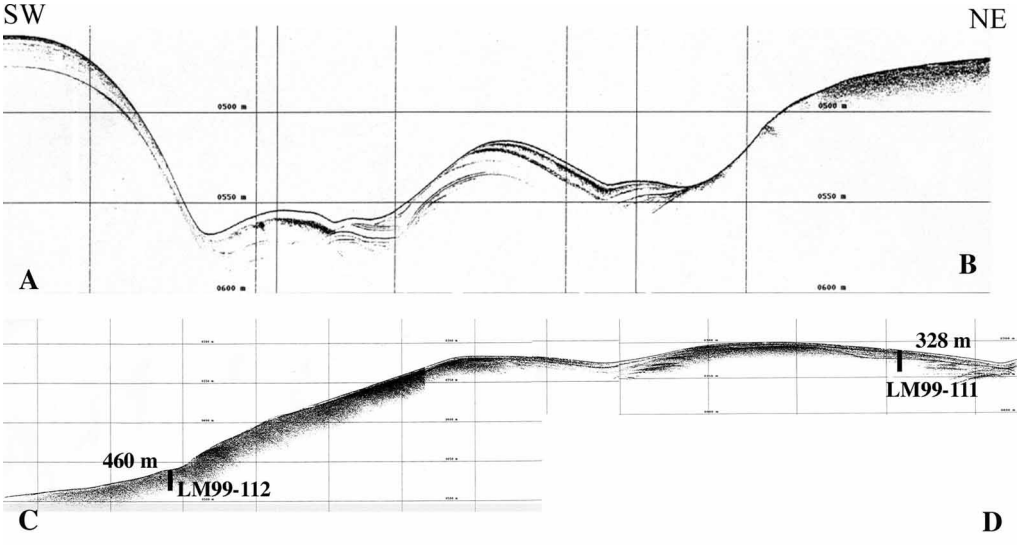

FIGURE 7 Chirp-sonar profiles across the Gorgona slope shown in Figure 1: C–D is the actual profile obtained during LM99-86 dredging; the position of cores discussed in the text is reported.

TABLE I Cruise LM99 Location and Attributes of Sampling Stations on the Gorgona Slope.

Stat.	*Lat. N*	*Long. E*	*Gear*	*Depth (m)*
49	43°24.6854	9°43.2638	Dredge	621 (begin)
	43°24.9373	9°43.7023		620 (end)
50	43°24.9451	9°44.6327	Dredge	536 (begin)
	43°25.1850	9°45.3380		438 (end)
51	43°25.1536	9°45.3825	Dredge	433 (begin)
	43°25.4195	9°46.4826		408 (end)
52	43°25.0711	9°51.0550	Grab	200
53	43°25.0401	9°57.0892	Grab	140
54	43°24.9849	9°56.5963	Grab	134
86	43°23.4097	9°45.7064	Dredge	474
	43°24.7532	9°46.6675		309
87	43°24.0267	9°47.2011	Dredge	335 (begin)
	43°24.2613	9°47.2608		283 (end)
88	43°16.8811	9°55.3475	Grab	305
89	43°16.5324	9°58.9716	Grab	172
90	43°21.0468	9°48.0685	Dredge	467 (begin)
	43°21.0904	9°49.6830		324 (end)
109	43°20.9265	9°43.0049	Dredge	552 (begin)
	43°19.7971	9°42.4823		457 (end)
110	43°23.5980	9°45.7572	Dredge	463 (begin)
	43°24.6727	9°46.6825		301 (end)
111	43°24.8832	9°46.6674	Gravity core	328
112	43°23.6193	9°45.7630	Gravity core	460
113	43°22.4599	9°54.0348	Grab	176
114	43°24.9671	9°57.0767	Grab	141
115	43°26.7585	9°59.4770	Grab	138
116	43°28.8245	9°55.4370	Grab	183
117	43°28.0282	9°52.5917	Grab	155
118	43°26.4306	9°50.5343	Grab	213

particles, obtained through grinding samples, were graded by stereoscopic microscope. Thin sections were studied under an optical microscope for petrographic observations and by means of an electronic microprobe and an energy-dispersive X-ray analyzer imaging system for chemical characterization. Microprobe analyses were performed using a CAMECA CAMEBAX microbeam equipped with 4 WDS with an accelerating voltage of 15 keV and a beam current of 15 nA. The analytical precisions under the analysis-operating conditions were: Sr ± 9%, Mg ± 20% and Na ± 20%. X-ray dot mapping was obtained by a CamScan MX2500, equipped with an EDAX system for microanalysis. The X-ray dot mapping technique is used to analyze the distribution of elements in an area of the sample. Primary electrons of the beam probe bombarding the specimen cause the atoms to take on a high-energy state. The excess energy can be released in the form of an X-ray with a wavelength that is characteristic of the atomic species from which it came, giving the possibility to identify which elements are present under the electron probe. With modern software, it is possible to collect a series of spectra for each point (pixel) analyzed by the electron beam probe, as it is scanned across the surface of the sample and an image analysis can be performed.

The X-ray dot mapping was used in conjunction with a backscattered electron image (BEI), the area of which corresponds exactly to the area of the maps. Using the BEI, each mineralogical phase is imaged, based on the atomic numbers of the elements that constitute those phases. Interaction of the high-energy electron beam with sample surfaces causes some high-energy electrons to be reflected or emitted back from the surface, where they are detected and used to form the image. The images are 8-bit gray scale and are composed of 256 separate shades from 0 for black and 255 for white. Different minerals are thus

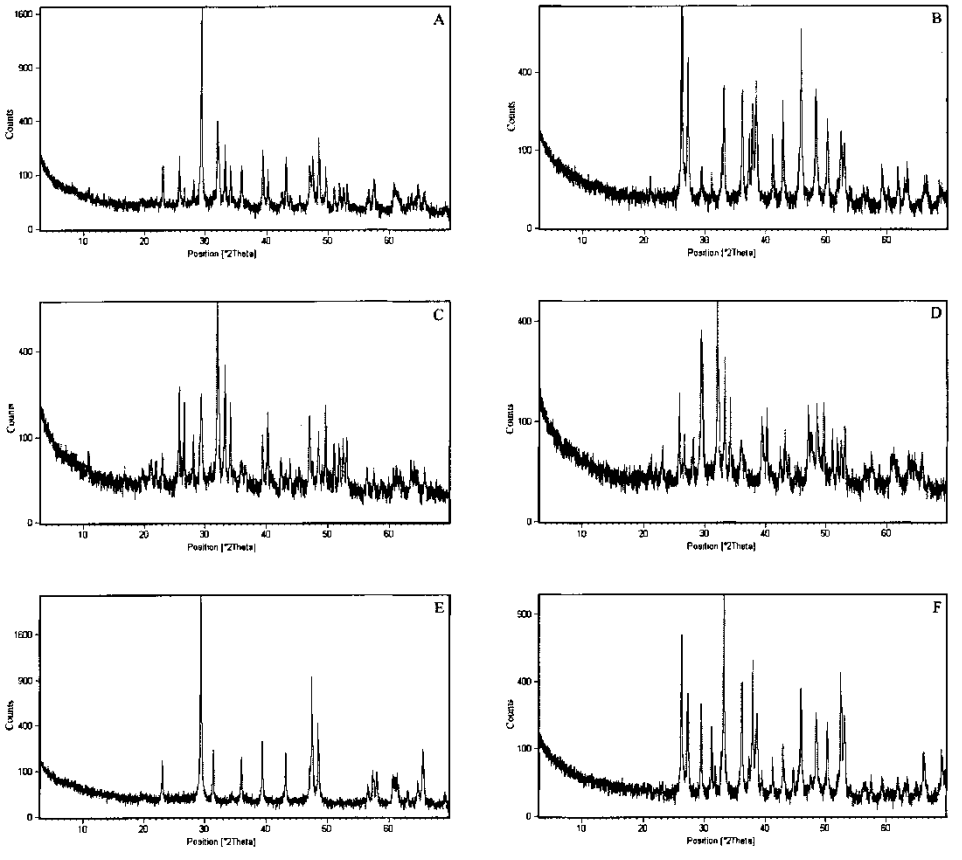

PLATE 1 X-ray diffraction patterns of various samples from the Gorgonia slope. (A) hardground; (B) *Caryophyllia smithii*; (C and D) bivalve mold; the two X-ray diffraction patterns were obtained analyzing two different parts of the bivalve mold; C shows the presence of goethite and a small amount of glaucony, whereas D reveals the presence of low-Mg calcite; (E) pristine Pleistocene bivalve; and (F) *Limnocardium* fragment.

represented by areas of varying shades of gray depending on their average atomic number; the higher the number, the brighter the shade.

3 RESULTS AND DISCUSSION

X-ray dot mapping was performed on hardground, Pleistocene skeletal parts and Messinian concretions, to study the chemical composition of the samples. Chemical maps provide a powerful tool to define the major and minor element distribution along the sample and allow recognition of heterogeneities that are otherwise difficult to observe.

3.1 Hardground

3.1.1 Petrography

The cemented crust consists of biomicrite with localized micrite. The biogenic component is largely represented by planktonic foraminifer tests, with minor amounts of bivalve and echinoid fragments (Plate 2(1,2)).

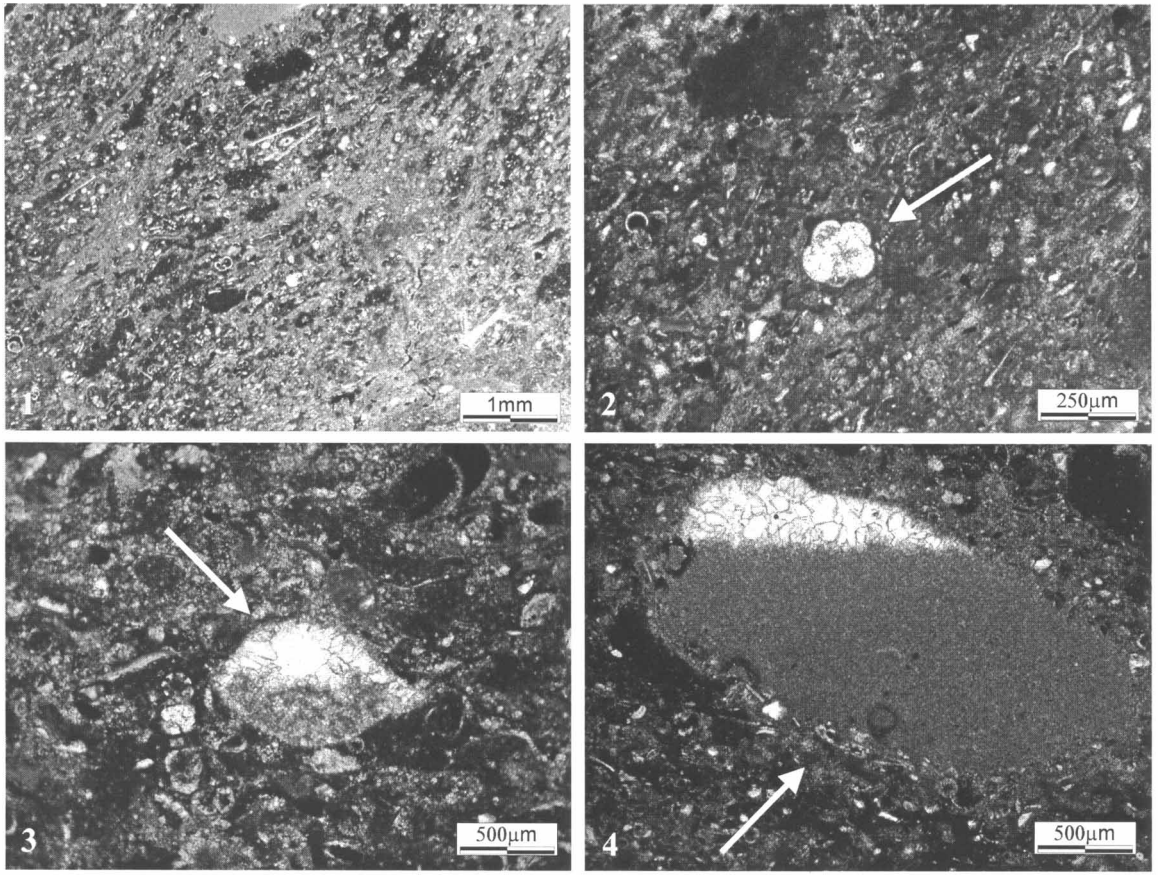

PLATE 2 (1) Biomicrite with localized micrite; the skeletal component consists of planktonic foraminifer tests, with minor amounts of bivalve and echinoid fragments. (2) Detail of the same sample; note planktic foraminifer (arrow). (3) Bivalve shell (arrow) partially filled by a micrite matrix and a sparitic blocky cement, forming a normal geopetal structure. (4) Normal geopetal structure.

The micrite shows a pseudo-peloidal texture characterized by areas with different crystalline degree. The intraparticle porosity of many skeletal parts and other nonbiogenic particles is partly filled by a micrite matrix and a sparitic blocky cement, frequently forming normal geopetal structures (Plate 2(3,4)). Diffractometric analysis revealed the presence of low-Mg calcite, hydroxyapatite, quartz and a mineralogical phase in agreement with a glaucony composition (Plate 1(A)). Odin and Létolle (1978) proposed the word glaucony to designate a green grains facies as a whole, ranging from an end-member which is a smectite (glauconitic smectite), to an end member which is a clay-size mica (glauconitic mica).

3.1.2 Geochemistry

The backscattered electron image (Plate 3(A)) shows chemical heterogeneities in the hardground section. Calcium distribution (Plate 3(1)) is basically homogeneous over the section, due to the high amount of calcium carbonate and calcium phosphate. Phosphorus has a similar distribution to that of calcium even though it is less continuous (Plate 3(2)). Silicon concentration reflects the distribution of silicate minerals and, in particular, the presence of quartz (Plate 3(3)). Finally, a very high concentration of iron is located along the rim of the hollow on the left side of the image, and it gradually decreases toward the carbonate phase (Plate 3(4)). The bright material with the highest iron concentration was analyzed using the EDAX system, and it contains about 63% iron (by weight), suggesting the presence of goethite. Taking into account all the chemical information derived from the X-ray dot mapping images, and also considering the potassium and aluminum distribution (Plate 3(5,6)), we sketched the area containing the glaucony phase (cross-hatched area in Fig. 8). Both the micritic matrix and the cement filling a bivalve shell (Plate 2(3)) were analyzed using an electron microprobe (Tab. II). The $MgCO_3$ content of the micritic phase ranges from 2 to 6.5 mol% whereas that of the cement ranges from 4.5 to 7 mol%. Similar results

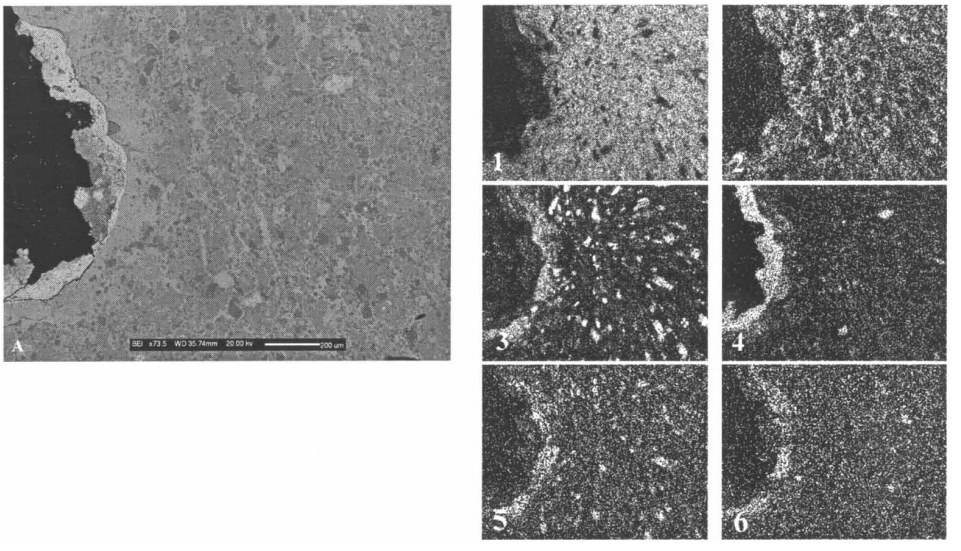

PLATE 3 (A) Backscattered electron image of the hardground. Different minerals are represented by areas of varying shades of gray depending on different average atomic number; the higher the number, the brighter the shade. 1–6: X-ray dot maps representing the distribution of some chemical elements. (1) Calcium; (2) phosphorus; (3) silicon; (4) iron; (5) aluminum; and (6) potassium. The brightest area on the left side of 4 is goethite (see Text). Note that the brightest areas correspond to the highest concentration of the element investigated.

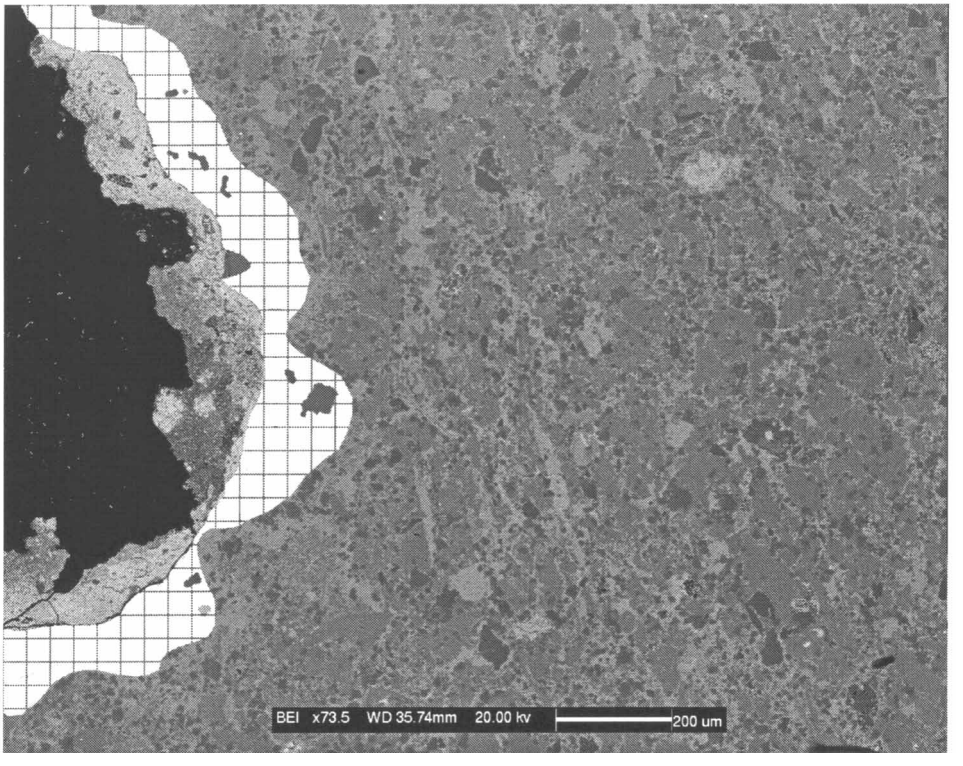

FIGURE 8 Backscattered electron image of the hardground. The cross-hatched area represents the glaucony phase. It was obtained by analyzing all the information coming from the X-ray dot mapping images in Plate 5. Most of the bright area between the hollow and the glaucony phase is goethite.

were obtained for both the micritic matrix and the cement in a carbonate grain (Plate 2(4)). Strontium concentration in the micritic matrix (Plate 2(3,4)) ranges from 500 to 1300 ppm, whereas in the cement (Plate 2(3,4)) the concentration is below the detection limit.

3.1.3 Discussion

The cemented carbonate sediment (hardground) studied could be considered a product of an early submarine diagenesis under nondepositional conditions.

The pre-existing pelagic sediment, rich in planktonic foraminifers, underwent a lithification process induced by the precipitation of a magnesian calcite. The cementation is referred to as a physicochemical process controlled by ionic diffusion from sea to interstitial waters (Allouc, 1990). Carbonate cement precipitation is mainly the effect of the very slow sedimentation rates, where the interaction between sediment and seawater can occur. Allouc (1990) subdivided the deep-sea Mediterranean crusts into three types, referring to a progressive cementation process from type 1 to type 3. Type 1 is described as a thin, brittle limestone, type 2 as a thick, rather stiff limestone, and type 3 as an almost entirely cemented crust. He observed a trend of progressive lithification and increasing high-magnesian calcite content from the incipient to the more evolved crusts. The $MgCO_3$ content of diagenetic high-Mg calcite for these crusts ranges between 9–10 and 12–13 mol%. The petrographic features of the upper crust we have analyzed correspond to an evolved crust, characterized

TABLE II Sodium, Magnesium and Strontium Concentrations Obtained Using an Electron Microprobe.

Sample	*Na (ppm)*	*Mg (W%)*	*Sr (ppm)*
MM (bivalve shell – hardground)	719	0.5984	725
MM (bivalve shell – hardground)	686	0.6592	573
MM (bivalve shell – hardground)	429	0.5895	1173
MM (bivalve shell – hardground)	731	0.9372	629
MM (bivalve shell – hardground)	2164	0.5424	1354
MM (bivalve shell – hardground)	749	1.8906	427
MM (bivalve shell – hardground)	918	1.5244	923
C (bivalve shell – hardground)	*	1.4795	*
C (bivalve shell – hardground)	*	1.8653	*
C (bivalve shell – hardground)	*	1.3123	*
C (bivalve shell – hardground)	*	2.0352	*
MM (carbonate grain – hardground)	956	1.192	629
MM (carbonate grain – hardground)	2765	1.308	701
MM (carbonate grain – hardground)	835	1.792	581
MM (carbonate grain – hardground)	516	0.6395	1037
MM (carbonate grain – hardground)	921	0.9472	938
C (carbonate grain – hardground)	*	1.3023	*
C (carbonate grain – hardground)	*	1.472	*
C (carbonate grain – hardground)	*	1.749	*
C (carbonate grain – hardground)	*	1.983	*
DA (Pleistocene *Astarte*)	1864	0.0227	748
DA (Pleistocene *Astarte*)	3156	0.0295	596
DA (Pleistocene *Astarte*)	2541	0.0286	608
DA (Pleistocene *Astarte*)	2607	0.007	2356
DA (Pleistocene *Astarte*)	2809	0.0068	1938
DA (Pleistocene *Astarte*)	2548	0.0002	2436
PR (Pleistocene *Astarte*)	3673	0.0227	785
PR (Pleistocene *Astarte*)	3521	0.0032	1728
PR (Pleistocene *Astarte*)	4706	0.0035	1375
PR (Pleistocene *Astarte*)	3677	0.0046	1843
PR (Pleistocene *Astarte*)	3261	0.0002	1888
PR (Pleistocene *Astarte*)	2967	0.0002	2539
C (Messinian concretion)	*	0.0896	*
C (Messinian concretion)	*	0.0966	*
C (Messinian concretion)	*	0.1156	*
C (Messinian concretion)	*	0.0837	*
C (Messinian concretion)	*	0.1063	*

Notes: MM – Micritic Matrix (see Plate 2); C – Cement (see Plate 2); DA – Diagenetically altered Pleistocene *Astarte* shell; PR – Pristine Pleistocene *Astarte* shell.
*Concentration below the detection limit.

in some areas by a pervasive cementation. The diagenetic cement has a fairly low $MgCO_3$ content compared to that found by Allouc (1990) for the evolved crusts. X-ray diffraction indicates a mean $MgCO_3$ content of about 4–5 mol% in the carbonate matrix. Our explanation to account for this depletion refers to the richness of the original host sediment in carbonate skeletal remains and also considers the effect of kinetics during the $MgCO_3$ incorporation into calcite. The hardground studied is a biomicrite, particularly rich in planktonic foraminifers (Plate 2), and the organic matter content in the sediment must have been high enough to create a slightly reduced environment that is not favorable for magnesian calcite precipitation. The presence of a glaucony phase and phosphates is also related to a negative Eh condition. In particular, glauconite is thought to precipitate in a slightly reducing, anoxic, non-sulfidic, post-oxic diagenetic environment (Berner, 1981). In this kind of environment, the conditions can change from oxic to anoxic relatively easily, and there is no sulfate reduction since the amount of organic matter is too low. The different chemical

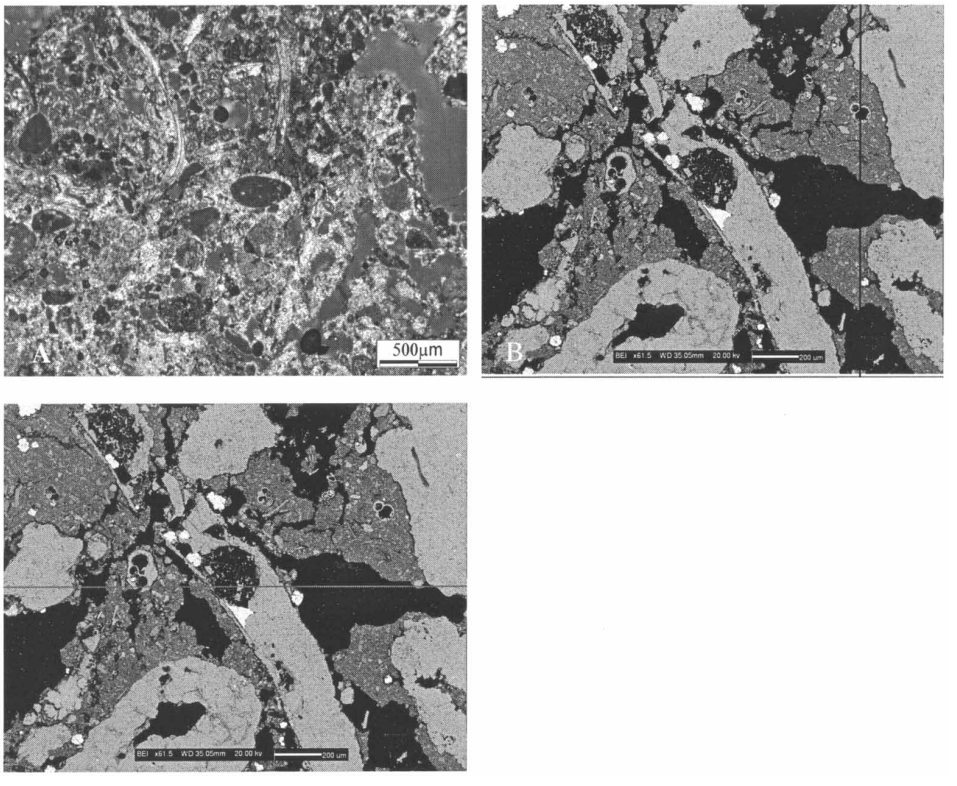

FIGURE 9 Messinian concretion. (A) Thin section showing the presence of both skeletal- and non-skeletal components. The skeletal component mainly consists of *Limnocardium* bivalve and fragments of planktonic foraminifer tests. (B) Backscattered electron image. Pyrite is easily detectable for its higher average atomic number compared to carbonate or silicatic minerals.

distribution observed in Figure 8 could be explained by an Eh fluctuation during diagenetic processes. The glaucony phase is a ferrous mineral that normally precipitates within sediments, in semi-confined environments, during early diagenesis and lack of deposition. These microenvironments are characterized by reducing conditions developed through bacterial decomposition of organic matter (Tucker, 1991). Bacterial reduction of iron oxides/hydroxides of clay and organic matter provide Fe^{2+} for glaucony phase development. The cross-hatched area in Figure 9 represents the glaucony phase, possibly a pre-existing detrital glaucony grain. Successive positive Eh conditions allowed the goethite to develop. In fact, goethite is also formed by oxidation and hydration of other iron minerals. The iron distribution map in Plate 3(4) gives the right size and position of goethite. It is exactly along the border of the hollow, and it seems to be the product of the alteration of the near glaucony phase. The organic matter (phosphate-rich tissues) also releases its contained phosphate during bacterial reduction. Phosphate does not seem to precipitate directly from sea water but it is formed below the sediment–water interface, by replacement and impregnation of grains (Soudry and Champetier, 1983; Lucas and Prevot, 1985). Moreover, the environment must not be overly reductive, otherwise bacterial reduction of the organic matter is inhibited (Tucker, 1991). The phosphorus distribution map in Plate 3.2 is clear evidence of the phosphatization of the carbonate sediment. Considering the presence of the glaucony phase and the impregnation of carbonate sediment by phosphate, it appears that the sediment underwent a diagenetic process in the presence of fertile water and Eh fluctuations. As

pointed out by Allouc (1985, 1986a), magnesian calcite concentrations are low in more fertile waters. Another reason for the low $MgCO_3$ content in the crust under study, particularly referring to diagenetic cement, could be the kinetics of calcite precipitation processes. In particular, it has been proven that the incorporation of $MgCO_3$ in calcite increases with increasing precipitation rate (Thorstenson and Plummer, 1977; Wollast *et al.*, 1980). The precipitation rate decreases in the quasi-isolated interstitial water offered, for example, by biogenic cavities. Larger, subhedral to euhedral diagenetic crystals precipitate in these microenvironments (as observed in Plate 2(3)) and the $MgCO_3$ content is lower compared to small crystals formed by a high precipitation rate.

3.2 Pleistocene Skeletal Parts

3.2.1 Petrography

(1) Two shell fragments of the bivalve mollusc *Astarte sulcata* were studied under optical microscope using valve cross-sections (thin sections) and by means of a SEM in fractured sections. Petrographic observations reveal pristine microstructures of both shell fragments. The innermost layer consists of an aragonitic irregular simple prismatic layer (Plates 4(1,2) and 5(2,3)) with variable thickness, ranging from about 100 μm to 1 mm.

Along this layer, thin-branched bores are evident only in one shell fragment (Plates 4(2) and 5(3,4)). These bores range from 10–15 μm to 30 μm in diameter and are partially or completely filled. Similar branched bores can be observed in the outer layer. This layer consists of an aragonitic spherulitic prismatic structure and it seems to have been more affected by endobenthic activity (microboring, *Trypanites* ichnofacies) compared to the innermost layer. In the other shell fragment, the distribution of branched bores is limited, and they normally do not contain any filling material (Plates 4(1) and Plate 5(1,2)).

(2) Transverse sections of a solitary scleractinian coral *Caryophyllia smithii* were studied using an optical microscope and a SEM. The coral reveals pristine microstructures in both the wall and columella regions. The aragonite fibrous bundles do not show significant dissolution features (Plates 4(3) and 5(5,6)). Calcification centers, arranged in a continuous line parallel to the septal surface (Plate 5(5,6)), are completely absent in some septal portions (Plate 4(3,4)). This is related to the smaller size of the crystals that form the calcification center itself, making it more sensitive to dissolution processes. Along the external side of the coral wall, branched microboring comparable to that observed on the shell of *A. sulcata* is present, and these bores are partially or completely filled. Diffractometric data confirmed the aragonitic composition of the coralline skeleton (Plate 1(B)). Because of the scarcity of material filling the bores (in agreement with a glaucony composition; see below), its mineralogy was not ascertained.

3.2.2 Geochemistry

The innermost layer of pristine shell fragment of *A. sulcata* displays an almost homogeneous calcium distribution (Plate 6(1)), due to the small number of bores. There is no evidence of silicon, aluminum and iron enrichment along the layer (Plate 6(2–4)). This is different from the other fragments, where the branched bores along the innermost layer are completely filled. The filling material is characterized by a high silicon, aluminum and iron concentration (Plate 7(2–4)). We obtained the same element distribution in our analysis of the fragment of *C. smithii* (Plate 8). The bores here show a similar geometry to that observed in the *A. sulcata* layer and the filling material appears to be the comparable.

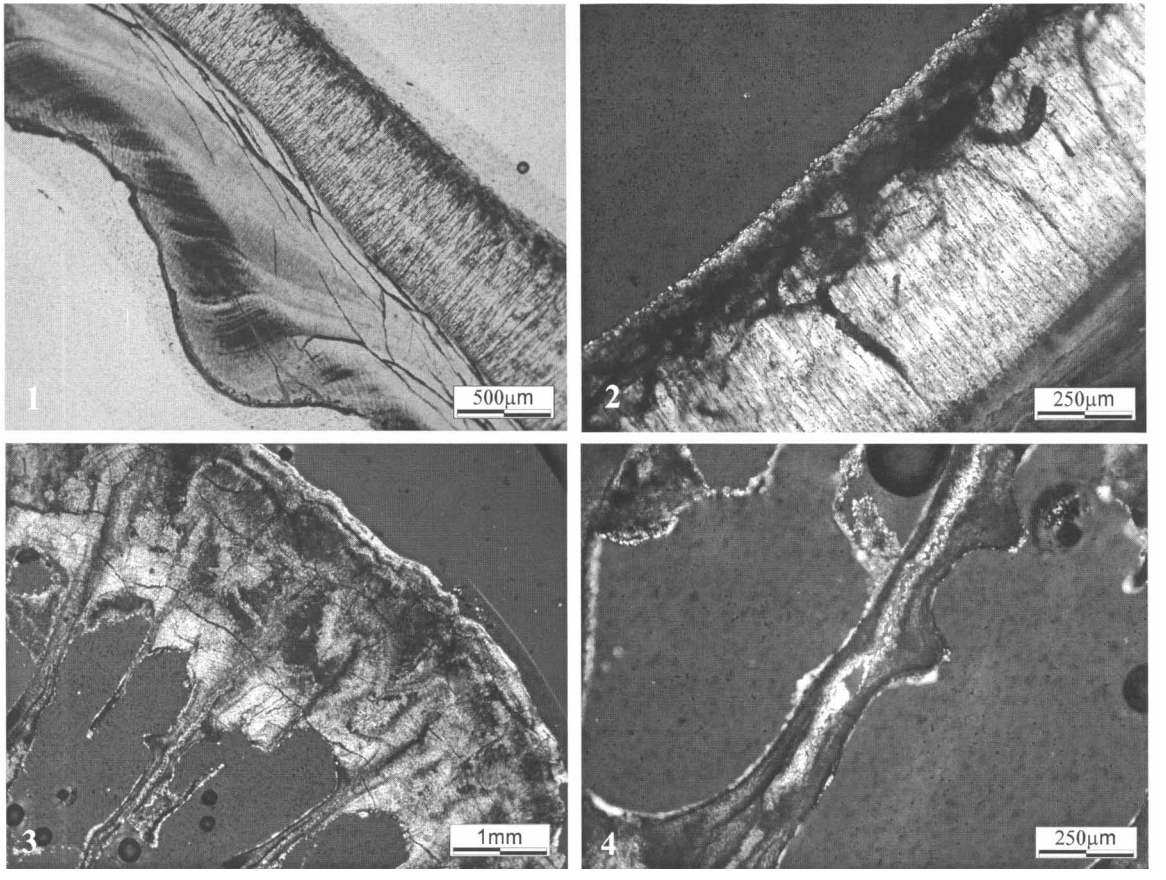

PLATE 4 (1) Pleistocene pristine shell of *A. sulcata*. Microboring is absent both in the outer and in the inner shell layers. (2) Pleistocene diagenized shell of *A. sulcata*. The innermost layer shows the presence of microboring filled with glaucony. (3) Cross-section of *C. smithii*, showing the wall region and part of the septal portion. (4) Detail of a septum in *C. smithii*. Calcification centers developed along the septum have been completely removed by dissolution processes.

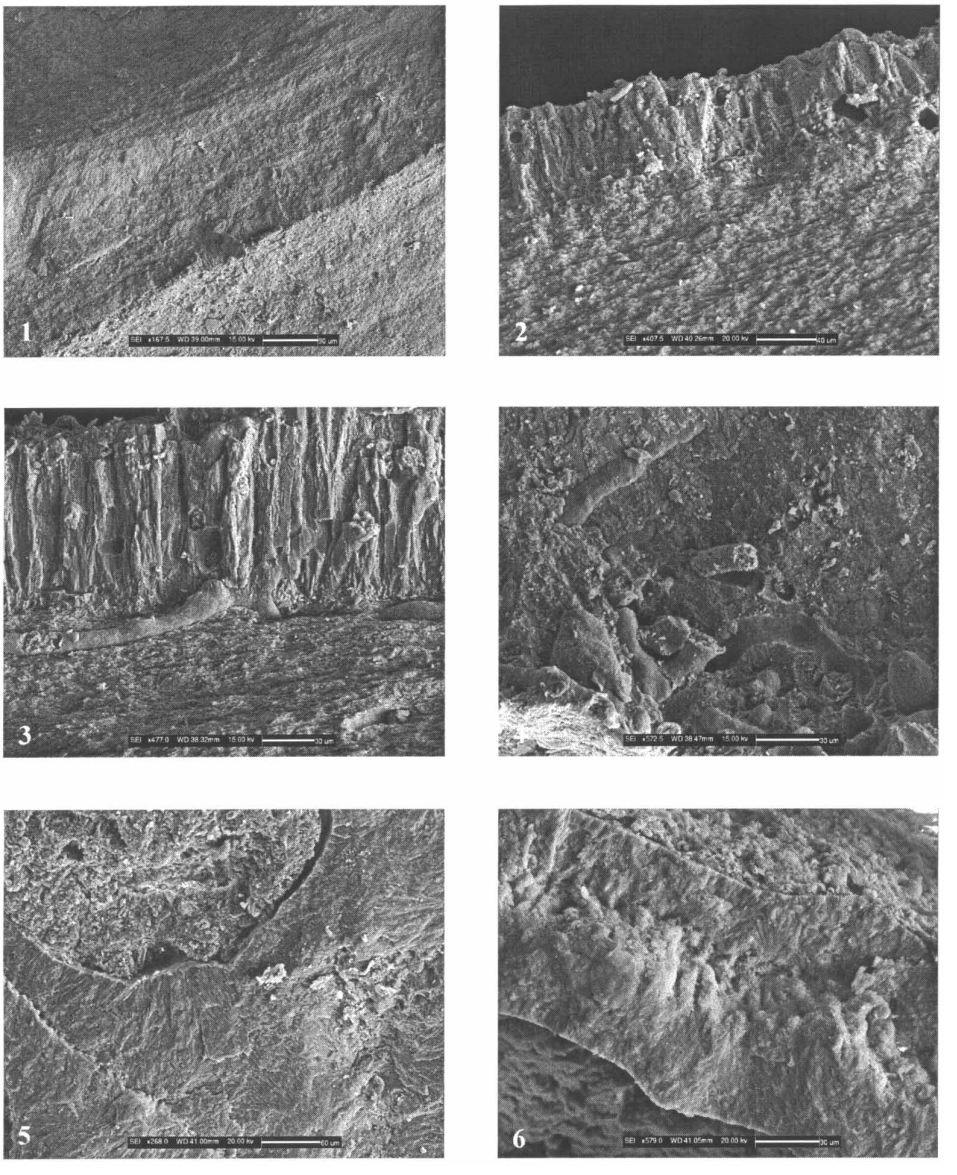

PLATE 5 (1) Outer shell layer of *A. sulcata.* This layer shows pristine structures and the distribution of microboring is limited. (2) Innermost shell layer of *A. sulcata.* This layer consists of an aragonitic irregular simple prismatic layer. Microburrows do not contain any filling material. (3) Detail of the innermost layer showing the distribution of branched bores and the filling material. (4) Detail of branched bores and the filling material. (5) Wall region and outer septal portion of *C. smithii.* The coral reveals pristine microstructures. The inter-septal porosity is completely or partially filled by clay minerals and quartz silt. (6) Detail of a septum in *C. smithii.* Calcification centers are arranged in a continuous line parallel to the septal surface and are surrounded by fibrous aragonitic bundles.

Moreover, a potassium and magnesium enrichment was also found for the filling material of both *A. sulcata* (Plate 7(5,6)) and *C. smithii* (Plate 8(5,6)). Major and minor element concentrations of the material filling the microboring are in agreement with a composition of a glaucony phase. Analytical cross-sections were carried out between the outermost and the innermost shell layers of *A. sulcata* (Tab. II). Information for strontium, magnesium and

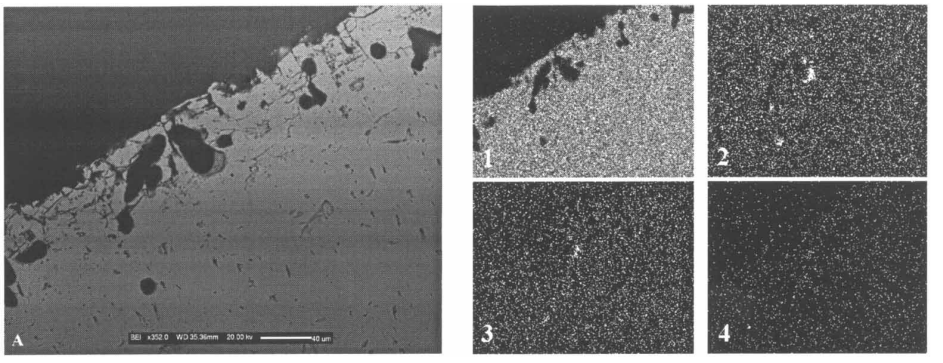

PLATE 6 (A) Backscattered electron images of the shell of *A. sulcata.* Different minerals are represented by areas of varying shades of gray depending on the different average atomic number; the higher the number the brighter the shade. 1–4: X-ray dot maps representing the distribution of some chemical elements. (1) Calcium; (2) silicon; (3) aluminium; and (4) iron. Note that the brightest colored areas correspond to the highest concentration of the element investigated.

sodium only concern the carbonate phase, since the filling material was carefully avoided. Although analytical precision for the selected elements is quite high, it is possible to notice geochemical differences among the various portions of the samples. Results for magnesium are given in Figure 10. The two magnesium distributions derived from the two shell cross-sections are quite different. Regarding the shell with no branched microboring (Fig. 10A), the magnesium concentration is almost homogeneous, with the exception of the high magnesium value in the outermost shell layer (1 on the analytical points axis). The other shell of *A. sulcata* shows a different magnesium distribution (Fig. 10B). Anomalous high values were observed in the outer part of the shell.

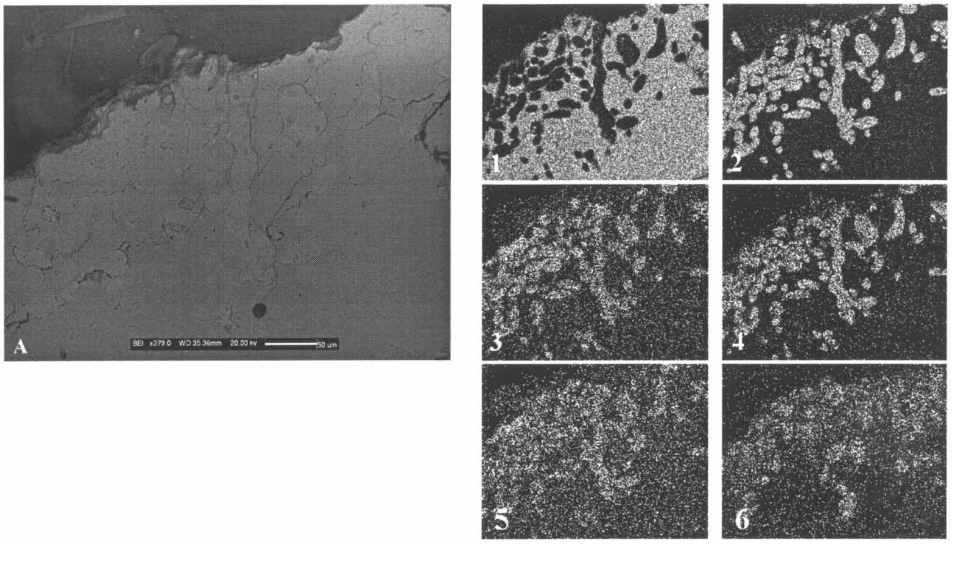

PLATE 7 (A) Backscattered electron image of the shell of *A. sulcata.* Different minerals are represented by areas of varying shades of gray depending on the different average atomic number; the higher the number, the brighter the shade. 1–6: X-ray dot maps representing the distribution of some chemical elements. (1) Calcium; (2) silicon; (3) aluminum; (4) iron; (5) magnesium; and (6) potassium. Note that the brightest areas correspond to the highest concentration of the element investigated.

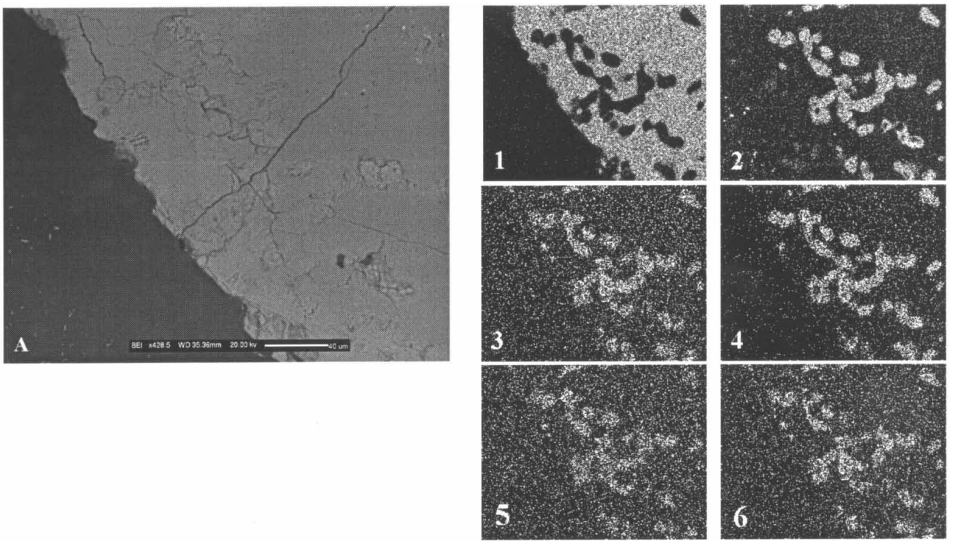

PLATE 8 (A) Backscattered electron image of *Caryophyllia* wall. Different minerals are represented by areas of varying shades of gray depending on the different average atomic number; the higher the number, the brighter the shade. 1–6: X-ray dot maps representing the distribution of some chemical elements. (1) Calcium; (2) silicon; (3) aluminum; (4) iron; (5) magnesium; and (6) potassium. Note that the brightest areas correspond to the highest concentration of the element investigated.

Strontium concentration displays an antithetic magnesium distribution over both the cross-sections, and low values correspond to the highest magnesium value. By applying an inferential statistical method, we achieved the main goal of finding out significant differences between the elemental compositions of the two shells. We adopted the NPC (NonParametric Combination) Test methodology (Pesarin, 2001) because of the partially nonnormal nature of our data. We found a significant difference (at the 5% level) between the two shells only for sodium concentration (Fig. 11).

3.2.3 Discussion

Petrographic and geochemical data allow us to define the differences between the two shells of *A. sulcata* and derive information on diagenetic processes. The two shells represent an initial and a successive step in the diagenetic sequence respectively. In particular, the shell without or with microboring shows an almost constant concentration of magnesium over the whole shell's thickness. The magnesium peak in the outermost layer seems to be indicative of an incipient slight replacement of the primary aragonite by a diagenetic calcite. This process is more evident in the other shell, since the entire outer layer shows magnesium enrichment. Moreover, high magnesium values correspond to the lowest strontium values. The partial replacement of aragonite by a diagenetic calcite seems to occur in the outer layer. This replacement is confirmed by the diffractometric data that reveal a slight amount of calcite in this shell. The large number of bores probably allowed the diagenetic solution to enter into the layer, thus creating the conditions for a mineralogical replacement. The chemical composition of the subsequent filling material is in agreement with a glaucony phase. As already discussed above, the glaucony phase is indicative of precipitation in a semi-confined environment and lack of deposition.

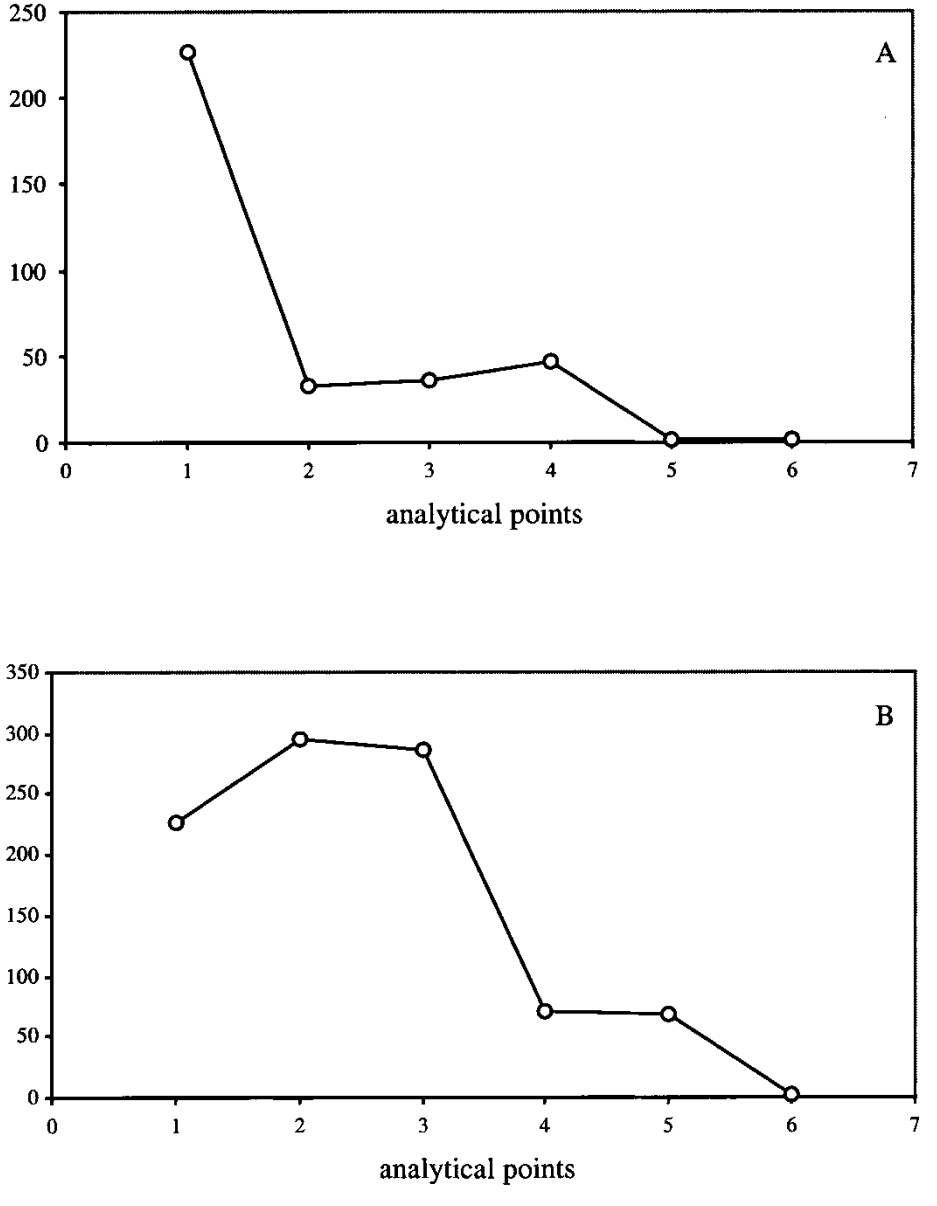

FIGURE 10 Distribution of Mg from the outermost to the innermost layer of *A. sulcata* shell, measured with the electronic microprobe along the aragonitic phase. The specimen without the microboring (A) has an almost homogeneous distribution with the only exception of the high Mg value for the first analytical point (outermost shell layer). The specimen with the microboring (B) shows a Mg enrichment in the outer shell layer (1–3).

The significant statistical difference in the sodium concentration between the two shells also provides evidence of a moderate calcitization process. Sodium concentration in aragonite is ~4000 ppm, whereas it is much lower in low-Mg calcite (~500 ppm) (Milliman, 1974a,b). Based on these data, the low sodium values in the diagenetically altered shell may be the effect of the calcitization process.

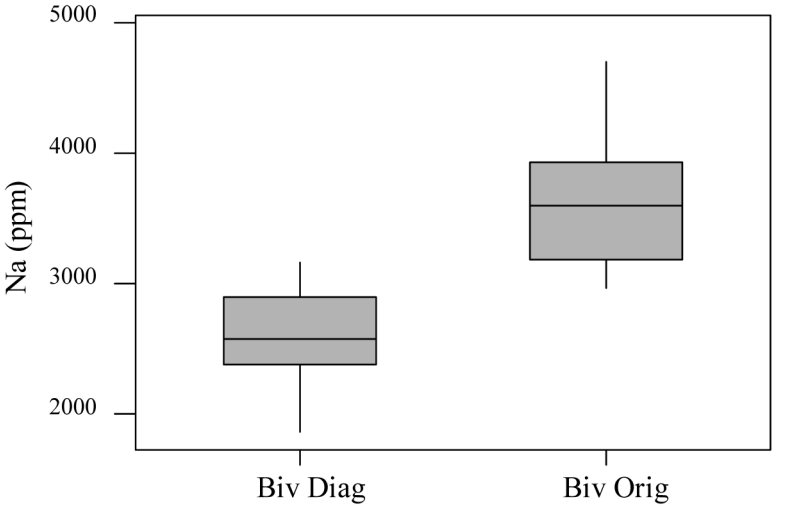

FIGURE 11 Graph showing the sodium concentration for the two shells. Biv Diag: diagenetically altered shell; Biv Orig: pristine shell.

3.3 Mold and Concretion

3.3.1 Bivalve Mold

3.3.1.1 *Petrography* The sample in Figure 7 is a bivalve plus matrix *steinkern* belonging to a distinct class of molds (black molds) represented by gastropods, scaphopods, bryozoans, brachiopods and scleractinian corals of unspecified Pleistocene age. This sample was sectioned and analyzed under optical microscope. It consists of a cryptocrystalline matrix (crystal diameters smaller than 1 μm), characterized by a brownish material when observed in thin section. Due to its high phosphorous content it can be defined as a phosphomicrite. Diffractometric analysis revealed the presence of hydroxyapatite, low Mg calcite, quartz, goethite and a small amount of glaucony, whereas a calcitic composition was obtained by analyzing a pristine Pleistocene bivalve (Plate 1(C–E)).

3.3.1.2 Discussion The *steinkern* examined represents an evolved phase of the diagenetic process. Some pristine shell remains underwent a replacement process, resulting in the complete phosphatization of the original shell. Moreover, as previously mentioned, the presence of glaucony, low-magnesium calcite and goethite, and the high amount of hydroxyapatite in the *steinkern* are indicative of a diagenetic process in the presence of fertile waters and Eh fluctuations.

3.3.2 Messinian Concretion

3.3.2.1 Petrography The sand-size portion of the Messinian concretion consists of bioclasts (chiefly bivalve fragments of *Limnocardium*), some peloids (many are probably fecal pellets), rock fragments and quartz grains (Fig. 8). The silt-size portion is essentially made up of clay minerals, planktonic foraminifer tests, quartz micrograins and subordinate pyrite microcrystals (normally pyrite framboids). The primary porosity is locally filled by a phosphomicrite. The carbonate cement occurs as an irregular isopachous fringe, chiefly around peloids and locally along grain contacts. Most of the biogenic elements (in particular

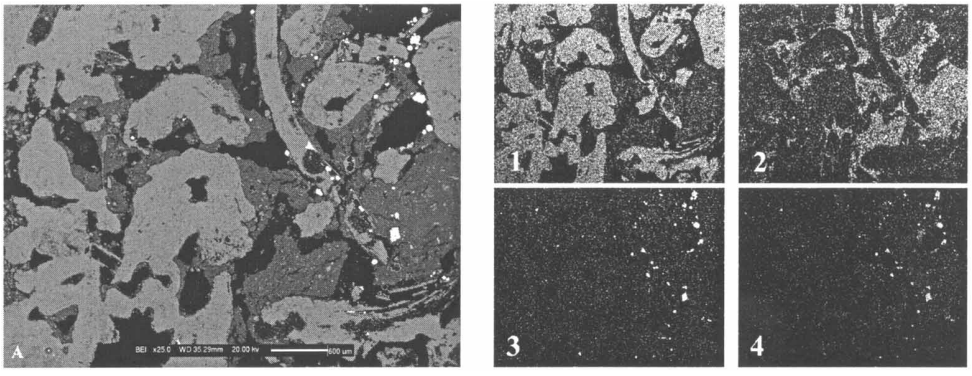

PLATE 9 (A) Backscattered electron image of the Messinian concretion. Different minerals are represented by areas of varying shades of gray depending on the different average atomic number; the higher the number the brighter the shade. 1–4: X-ray dot maps representing the distribution of some chemical elements. (1) Calcium; (2) silicon; (3) sulphur; (4) iron. Note that the brightest areas correspond to the highest concentration of the element investigated.

foraminifers) are empty and only some of them are partially filled by pyrite microcrystals or terrigenous fraction. The preservation of the *Limnocardium* fragments is highly variable, including both well-preserved biosomes and completely dissolved or calcitized skeletal parts. Diffractometric analysis of a chalky shell reveals the presence of aragonite (about 90%), calcite (8–9%) and hydroxyapatite (Plate 1F).

3.3.2.2 Geochemistry A backscattered electron image (Plate 9A) reveals the presence of high average atomic number minerals (bright crystals on the right area of the image in Plate 6A. The sulfur and iron distributions (Plate 9(3,4)), are in agreement with the petrographic observations, confirming the pyritic nature of the bright crystals in Plate 6A. Chemical maps of calcium and silicon distributions (Plate 9(1,2)) also confirm the presence of carbonate materials embedded in a matrix mainly composed of clay minerals and quartz silt. The $MgCO_3$ content of the isopachous carbonate cement is very low ($\sim$ 0.3–0.4 mol%) (Tab. II) compared to that found in the hardground, suggesting a different genesis.

3.3.2.3 Discussion Petrographic and geochemical features suggest a slightly different diagenetic process compared to those affecting the hardground and, to a lesser degree, the Pleistocene skeletons and molds. The amount of organic matter must have been adequate for sulfate reduction, creating an anoxic, sulfidic diagenetic environment. In such an environment, the bacterial reduction of sulfate in the presence of organic matter provides sulfur as S^{2-}, which forms pyrite together with iron. Pyrite, in the studied concretions, appears to precipitate within the silt-size portion and to replace small areas of the skeletal carbonates. Finally these concretions contain a mixed assemblage of skeletal grains including brackish Messinian bivalves and Pleistocene pelagic tests, indicating that their formation is a phenomenon that took place in a still unspecified time during the Quaternary.

4 CONCLUSIONS

Bottom samples of the Gorgona slope show phosphatized/micritc hardground and shell remains in various states of preservation. The starved deep-sea environment of the slope has favored diagenetic processes, promoting the partial or complete dissolution of existing

carbonates. Chemical precipitation and mineralization are evident in most samples belonging to Messinan and Pleistocene and were conducive to various types of lithified products, from glaucony- to phosphoritic-carbonate rocks. The chemical mapping of such varied diagenetic products provides a powerful tool for investigating chemical precipitation and mineralization, since an image analysis can be performed. X-ray dot mapping in conjunction with a BEI allowed us to show the different diagenetic patterns related to the varying amount of organic matter and Eh fluctuations. In particular, the cemented crust (hardground) and the Pleistocene skeletal parts seem to have experienced the same diagenetic processes, related to fertile water, in a slightly reducing, anoxic, nonsulfidic, post-oxic diagenetic environment, whereas the Messinian concretion underwent a lithification process in an anoxic, sulfidic diagenetic environment, where sulfate reduction could be promoted.

Acknowledgements

We are grateful to the Captain, officers, crew and colleagues aboard the R/V *Urania* during Cruise LM-99 (*Lophelia* – Millennium). This mission and subsequent study was funded through a CNR grant to M. T. We would also like to thank Federico Zorzi (Department of Mineralogy and Petrology, University of Padua) for technical support during diffractometric analyses, Fabio Tateo and Luca Peruzzo for useful discussions. English text was kindly revised by Zander Tripp. The SEM investigation and chemical analyses were performed at the Department of Mineralogy and Petrology of the University of Padova. Two unknown referees helped to improve the text. This is IGM scientific contribution no. 1376.

References

Aleria. (1980). Le canale de Corse et les bassins nord-tyrrhéniens au miocène supérieur et terminal (Messinien); leur évolution plio-quaternaire. *Géologie Méditerranéenne*, **7** (1), 5–12.

Allouc, J. (1985). Etudes sur la genèse et la signification paléohydrologique des encroûtements sous-marins de Méditerranée. *Thèse Doct. Etat*, Inst. Nat. Polytech. Lorraine, 454 + 32 pp.

Allouc, J. (1986). Les encroûtements sous-marins de Méditerranée orientale: une explication génétique. *Revue de l'Institute Français du Pétrole*, **41** (3), 351–376.

Allouc, J. (1990). Quaternary crusts on slopes of the Mediterranean Sea: A tentative explanation for their genesis. *Marine Geology*, **94**, 205–238.

Bacini Sedimentari. (1979). Primi dati geologici sul Bacino della Corsica (Mar Tirreno). *Atti del Convegno Scientifico Nazionale*, Roma, 5–7 Marzo 1979, pp. 713–727.

Baturin, G. N. (1981). Phosphorites on the seafloor. Origin, composition and distribution, in: *Developments in sedimentology.* Elsevier, Amsterdam, Vol. 33, 343 pp.

Benvenuti, M., Bertini, A. and Rook, L. (1994). Facies analysis, vertebrate paleontology and palynology in the late Miocene Baccinello-Cinigiano basin (Southern Tuscany). *Memorie della Società Geologica Italiana*, **48**, 415–423.

Benvenuti, M., Bertini, A. and Rook, L. (2001). Mammal biochronology, UBSU and paleoenvironmental evolution in a post-collisional basin: Evidence from the late Miocene Baccinello-Cinigiano basin in Southern Tuscany, Italy. *Bollettino della Società Geologica Italiana*, **120**, 97–118.

Berner, R. A. (1981). New geochemical classification of sedimentary environments. *Journal of Sedimentary Petrology*, **51**, 359–365.

Bernoulli, D. and Mc Kenzie, J. (1981). Hardground formation in the hellenic trench: Penesaline to hypersaline marine carbonate diagenesis, in Dercourt, J. (ed), *Programme HEAT, Campagne submersible, Les fossés Helléniques*, 19 août–15 septembre 1979. *Publications du Centre National Pour l'Exploitation des Océans (CNEXO), Résultats des Campagnes à la Mer*, 23, pp. 197–213.

Bossio, A., Esteban, M., Giannelli, L., Longinelli, A., Mazzanti, R., Mazzei, R., Ricci Lucchi, F. and Salvatorini, G. (1978). Some aspects of the upper Miocene in Tuscany. *Messinian Seminar Vol. 4, Field trip guidebook*, pp. 88.

Brachert, T. C. and Dullo, W.-C. (1990). Correlation of deep sea sediments and forereef carbonates in the Red Sea: An important clue for basin analysis. *Marine Geology*, **92**, 255–267.

Brachert, T. C. and Dullo, W.-C. (1991). Laminar micrite crusts and associated foreslope processes, Red Sea. *Journal of Sedimentary Petrology*, **61**, 354–363.

Ghetti, P., Anadón, P., Bertini, A., Esu, D., Gliozzi, E., Rook, L. and Soulié-Märsche, I. (2002). The early Messinian Velona basin (Siena, central Italy): Paleoenvironmental and paleobiogeographical reconstructions. *Palaeogeography, Palaeoclimatology, Palaeoecology*, **187**, 1–33.

Gillet, S., Lorenz, G. H. and Woltersdorf, F. (1965). Introduction a l'étude du Miocène supérieur de la région de Baccinello (environs de Grosseto, Italie). *Bulletin du Service de la Carte Géologique d'Alsace et de Lorraine*, **18**, 31–42.

Groupe Escarmed. (1983). Exemples de sédimentation condensée sur les escarpements de la Mer Ionienne (Méditerranée orientale). Observations à partir du submersible 'Cyana'. *Revue de l'Institute Français du Pétrole*, **38** (4), 427–438.

Hofmann, P., Schwark, L., Brachert, T., Badaut, D., Rivier, M. and Purser, B. H. (1998). Sedimentation, organic geochemistry, and diagenesis of cores from the axial zone of the southern Red Sea: Relationships to rift dynamics and climate. In: Purser, B. H. and Bosence, D. W. J. (eds.), *Sedimentation and tectonics of rift basins: Red Sea-Gulf of Aden.* Chapman & Hall, London, pp. 483–507.

Lucas, J. and Prevot, L. (1985). The synthesis of apatite by bacterial activity: Mechanism. *Sciences Geologiques Mémoire* (Strasbourg), **77**, 83–92.

Magné, J., Orszag-Sperber, F., Pilot, M. D., Brebion, P. and Lauriat-Rage, A. (1977). Nouvelles données sur le Pliocène de Corse: le problème de la limite Miocène-Pliocène. *Bulletin du B.R.G.M.*, **2, 1** (3), 209–218.

Milliman, J. D. (1974a). *Marine Carbonates*. Springer, New York, 375 pp.

Milliman, J. D. (1974b). Precipitation and cementation of deep-sea carbonate sediments. In Inderbitzen, A. L. (ed.), *Deep-Sea Sediments. Physical and Mechnical Properties.* Plenum, New York, pp. 463–472.

Milliman, J. D. (1977). Interstitial waters of late Quaternary Red Sea sediments and their bearing on submarine lithification. *Kingdom of Saudi Arabia, Red Sea Research 1970–1975, Mineral Resources Bulletin*, **22-M**, i-iii + M1–M6.

Milliman, J. D. and Müller, J. (1973). Precipitation and lithification of magnesian calcite in deep-sea sediments of the Eastern Mediterranean Sea. *Sedimentology*, **20**, 29–45.

Odin, G. S. and Letolle, R. (1978). Les glauconies et aspects voisins ou confondus: Signification sédimentologique. *Bulletin de la Société Géologique de France*, **20**, 553–558.

Pesarin, F. (2001). *Multivariate Permutation Tests with Applications in Biostatistics.* John Wiley and Sons, Chichester, 408 pp.

Remia, A. and Taviani, M. (2003). Shallow-buried pleistocene *Madrepora-Desmophyllum* patch reefs on a muddy continental slope, Tuscan Archipelago, NE Tyrrhenian Sea. In: Freiwald, A. and Schulbert, C. (eds.), *Erlanger Geologische Abhandlungen. 2nd International Symposium on Deep Sea Corals, September 8th–13th 2003*, Erlangen.

Rezak, R. (1974). Deep-sea carbonates, in Inderbitzen, A. L. (ed.), *Deep-Sea Sediments. Physical and Mechnical Properties.* Plenum, New York, pp. 453–461.

Selli, R. (ed.) (1970). Ricerche geologiche preliminari nel Mar Tirreno. *Giornale di Geologia.* Serie 2°, 37-1969, 249 pp.

Shonting, D. H. and Bartolini, C. (1971). Santa Lucia Bank: A small seamount in the Ligurian Sea. *Archivio Oceanografia Limnologia*, **17** (2), 157–168.

Soudry, D. and Champetier, Y. (1983). Microbial processes in the Negev phosphorites (southern Israel). *Sedimentology*, **30**, 411–423.

Taviani, M. (1998). Axial sedimentation of the Red Sea Transitional Region (22°–25° N): Pelagic, gravity flow and sapropel deposition during the late Quaternary. In Purser, H. P. and Bosence, D. W. J. (eds.), *Sedimentation and Tectonics of Rift Basins: Red Sea – Gulf of Aden.* Chapman & Hall, London, pp. 467–480.

Taviani, M., Remia, A. and Sami, M. (2002). Ritrovamento di Messiniano in facies Lago-Mare e Pleistocene glaciale nei sedimenti condensati del canyon di Gorgona, Tirreno. *CoNISMa, III Convegno Nazionale sulle Scienze del Mare, Bari, 27–30 Novembre 2002, Riassunti*, 62.

Thorstenson, D. C. and Plummer, L. N. (1977). Equilibrium criteria for two component solids reacting with fixed composition in aqueous phase – example: the magnesian calcites. *American Journal of Science*, **277** (9), 1203–1223.

Tucker, M. E. (1991). *Sedimentary Petrology: An Introduction of the Origin of Sedimentary Rocks*. Second Edition. Geoscience Texts, Blackwell Science, 260 pp.

Von Rad, U. and Rösch, H. (1984). Geochemistry, texture and petrography of phosphorite nodules and associated foraminiferal glauconite sands (Chatan Rise, New Zealand). *Geologische Jahrbuch*, **D-65**, 129–178.

Wilber, R. J. and Neumann, C. A. (1993). Effects of submarine cementation on microfabrics and physical properties of carbonate slope deposits, Northern Bahamas. In: Rezak, R. and Lavoie, D. L. (eds.), *Carbonate Microfabrics.* Springer-Verlag, New York, pp. 79–94.

Wollast, R., Garrels, R. M. and MacKenzie, F. T. (1980). Calcite-seawater reactions in ocean surface waters. *American Journal of Science*, **280**, 831–848.